Electronic Supplementary Material (ESI) for Journal of Materials Chemistry A.

Supporting information

Integrative Preparation of Mesoporous Epoxy Resin-Ceramic Composite Electrolytes with Multilayer Structure for Dendrite-Free Lithium Metal Batteries

Mengjie Li, Hao Li, Jin-Le Lan*, Yunhua Yu*, Zhongjie Du, Xiaoping Yang

State Key Laboratory of Organic-Inorganic Composites, College of Materials Science and Engineering, Beijing University of Chemical Technology, Beijing 100029, China

* Correspondence to lanjl@mail.buct.edu.cn (J-L. Lan), yuyh@mail.buct.edu.cn (YH. Yu)

As seen in Fig. S1a,† the absorption at 914 cm^{-1} attributed to the epoxy groups in two films almost disappeared, indicating that the epoxy resin was completely cured under the curing condition. When using D230 as the curing agent, a smooth-surfaced and translucent film was obtained after it was totally dried (Fig. S1b†). However, film cured by PACM was completely opaque and the significant differences in transparency of films with two curing agents can attribute to the different phase separation size. Fig S1c† and d† showed the differences in microstructure of the two films under the same magnification. It was seen that there were many interconnected polymer beads and some of them aggregated into large clusters, constituting the skeletal structure of the gel electrolyte when using PACM as the curing agent. The aperture of the membrane can be up to 4 μm, which led to the poor mechanical property and high ionic conductivity at room temperature (1.38×10^{-3} S cm^{-1} , Fig. S2†) of the sample. The pore size of the epoxy resin porous membrane with D230 as the curing agent was around 30-40 nm, which indicated that the network structure of the membrane was more uniform and compact, thus greatly improved the mechanical performance, but reduced the ionic conductivity (5.66×10^{-4} S cm^{-1} , Fig. S2†) compared with EME using PACM as the curing agent.

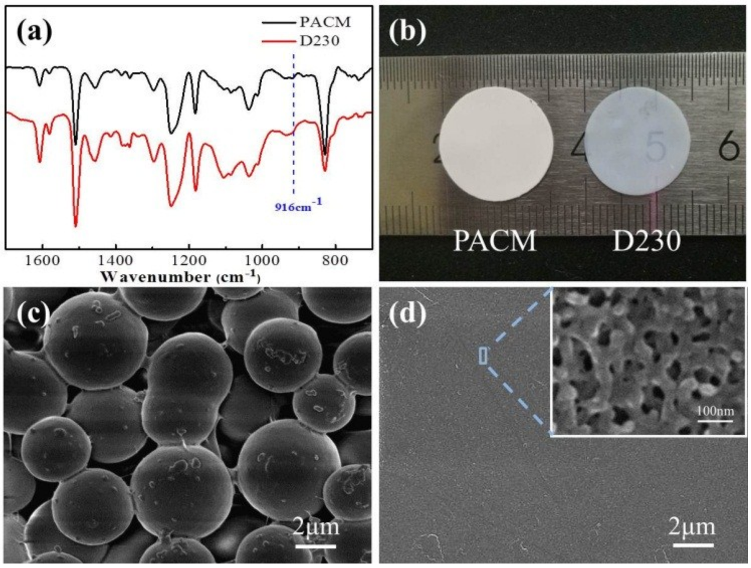

Fig. S1 (a) FTIR spectra and (b) optical photograph of epoxy resin porous membranes with two different curing agents. SEM images of EME-3 membranes with curing agent (c) PACM and (d) D230 after extraction of the pore-forming agent.

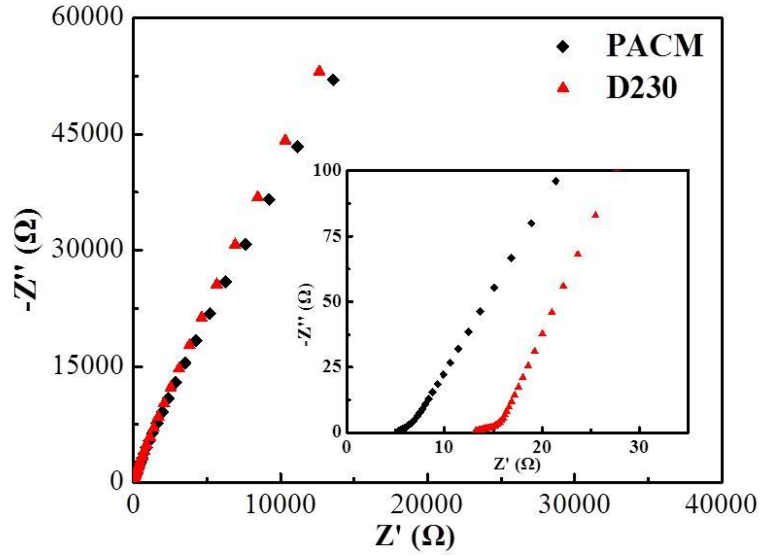

Fig. S2 Impedance spectra of SS/EME-3/SS cells with two different curing agents.

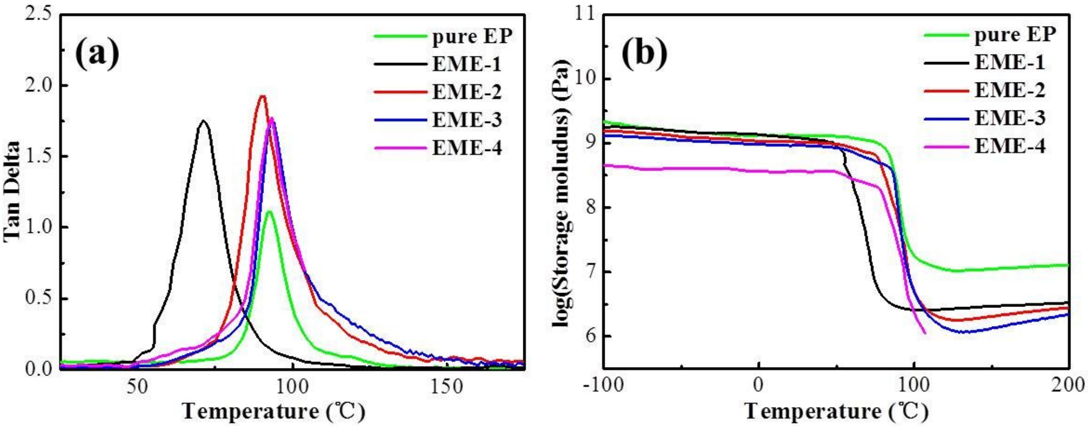

Fig. S3 DMA curves of EMEs membranes with different contents of PEG200 (before activation of liquid electrolyte)

Table S1 The DMA results of the epoxy matrix samples with different PEG200 contents

Sample label	Glass transition temperature (°C)	Storage modulus (MPa)	Cross-linking degree (mol·cm^{-3})
Pure epoxy	93	10.58	3.14×10^{-3}
EME-1	71	2.70	8.45×10^{-4}
EME-2	91	1.85	5.51×10^{-4}
EME-3	94	1.18	3.48×10^{-4}
EME-4	93	-	-

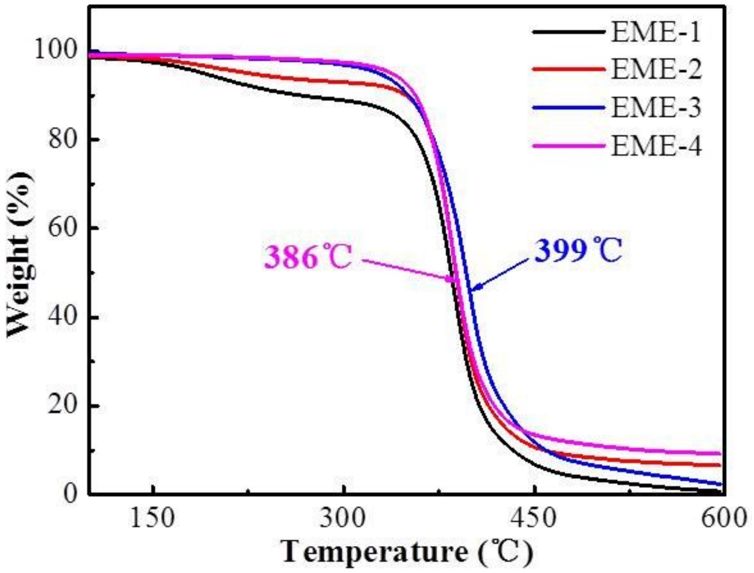

Fig. S4 TGA thermograms of EMEs membranes with different contents of PEG200 (before activation of liquid electrolyte)

Fig. S4† shows the thermos-gravimetric analysis (TGA) curves of the epoxy matrix membranes after different contents of PEG200 removed. The result of TGA reveals that EME-3 and EME-4 membranes are thermally stable up to 340 °C, but EME-1 and EME-2 membranes yield an obvious weight loss of 13% and 8% at 340 °C, respectively. These results may be caused by the thermal decomposition of the residual PEG200 in EME-1 and EME-2 membranes. Due to the greater cross-linking degree of the two systems, it makes it difficult to remove all the pore-forming agent and some PEG remained in the samples even after washing thoroughly. From the DMA results in Fig. S3,† we can find that the glass-transition temperature of EME-1 and EME-2 membranes decreased 22 °C and 2 °C respectively, compared with pure epoxy sample, but there were no attenuation for EME-3 and EME-4 membranes. This result is consistent with our above guess.

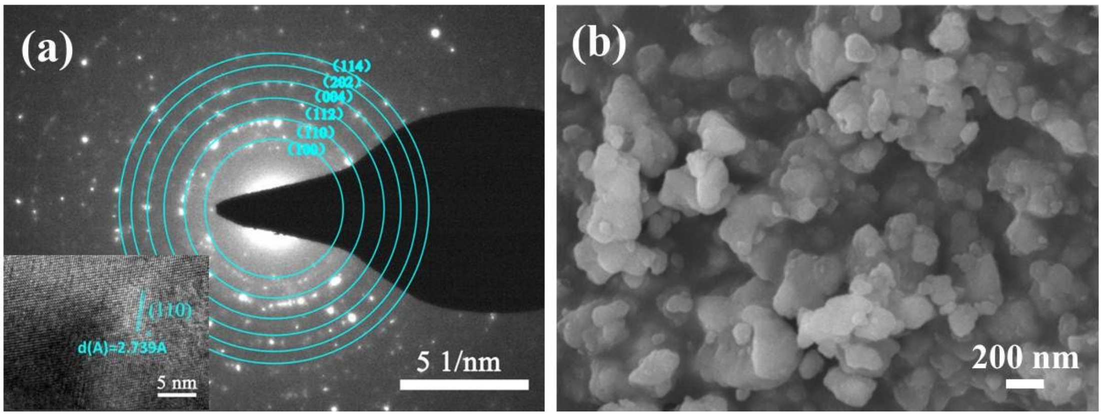

Fig. S5 (a) Corresponding SAED pattern with inset HRTEM image of an individual LLTO nanoparticle. (b) SEM image of LLTO ceramic powers.

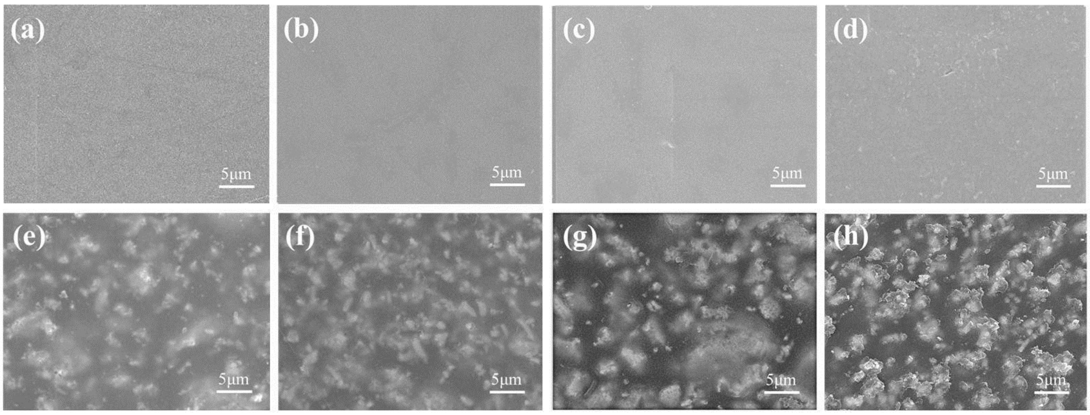

Fig. S6 SEM images of the top of the membranes of (a) c-EME-5%, (b) c-EME-10%, (c) c-EME-15%, (d) c-EME-20% and the bottom part of the membranes of (e) c-EME-5%, (f) c-EME-10%, (g) c-EME-15%, (h) c-EME-20%. (all samples are after extraction of the PEG200 and before infiltration liquid electrolyte)

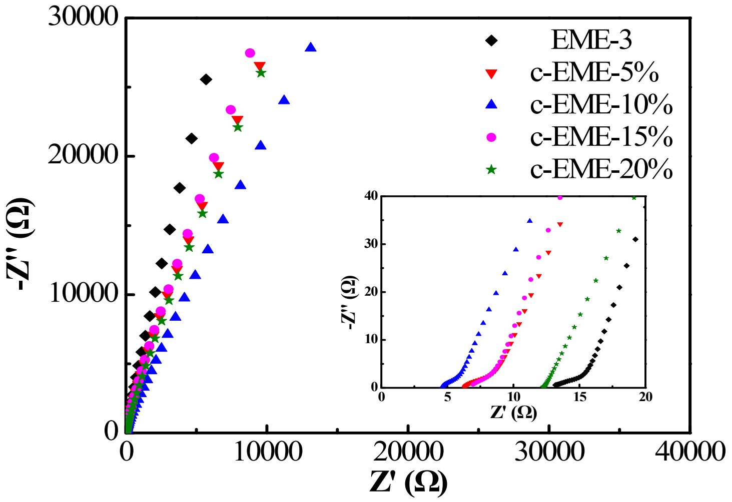

Fig. S7 Impedance spectra of SS/GPE/SS cells employing EME-3, c-EME-5%, c-EME-10%, c-EME-15% and c-EME-20%

Table S2 Effect of the LLTO nanoparticles content on the tensile strength, ionic conductivity and electrolyte uptake amount of the epoxy matrix samples

Sample label	**Tensile strength (MPa)**	**Ionic conductivity (S·cm^{-1})**	**Electrolyte uptake (%)**
EME-3	9.935	5.66×10^{-4}	272.3
c-EME-5%	16.00	1.18×10^{-3}	292.1
c-EME-10%	18.38	2.02×10^{-3}	352.9
c-EME-15%	20.48	1.07×10^{-3}	377.1
c-EME-20%	12.16	6.09×10^{-4}	384.3

As shown in Fig. S8, significant reduction and oxidation peaks between -1 V and 1 V were observed in three cells, indicating the plating and stripping of Li$^+$ onto/from stainless steel. In the anodic scan, there were current peaks at around 4.1 V and 4.5 V (vs. Li$^+$/Li) for EME-3 and Celgard 2400 respectively, which were mainly attributed to oxidative decomposition of the liquid electrolyte. For c-EME-10%, it showed a higher decomposition potential, which was consistent with linear sweep voltammetry (LSV) results. Furthermore, compared with EME-3, no additional current peak was observed near 1.5 V (vs. Li$^+$/Li) for c-EME-10%,[1,2] indicating that the three-tier structure in c-

EME-10% can avoid direct contact between LLTO and Li metal.

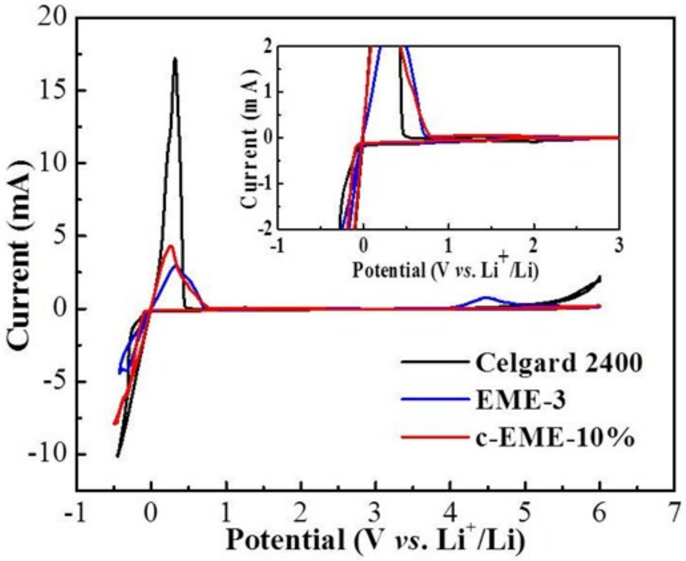

Fig. S8 Cyclic voltammetry of Li-SS cells using Celgard 2400-liquid electrolyte, EME-3 and c-EME-10% as the electrolytes.

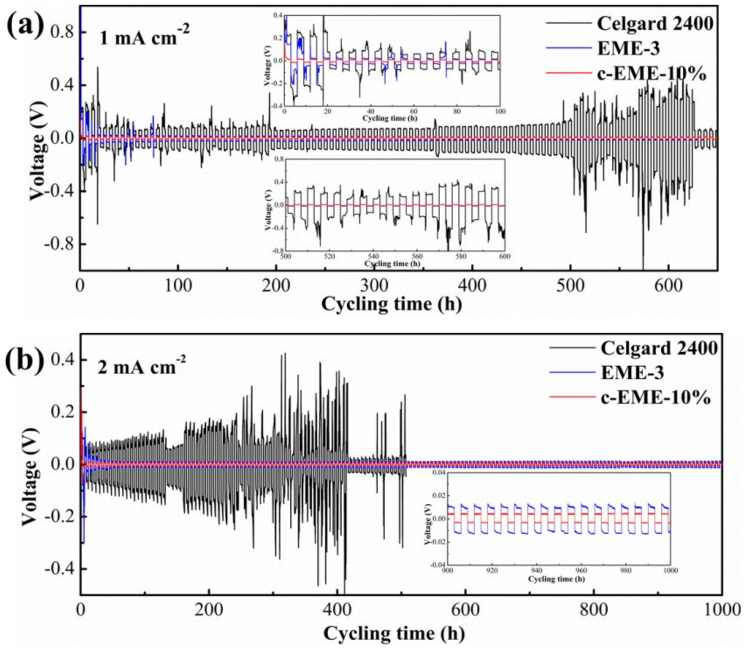

Fig. S9 Voltage profiles for Celgard 2400-liquid electrolyte, EME-3 and c-EME-10% at a current density of (a) 1 mA cm^{-2} and (b) 2 mA cm^{-2}.

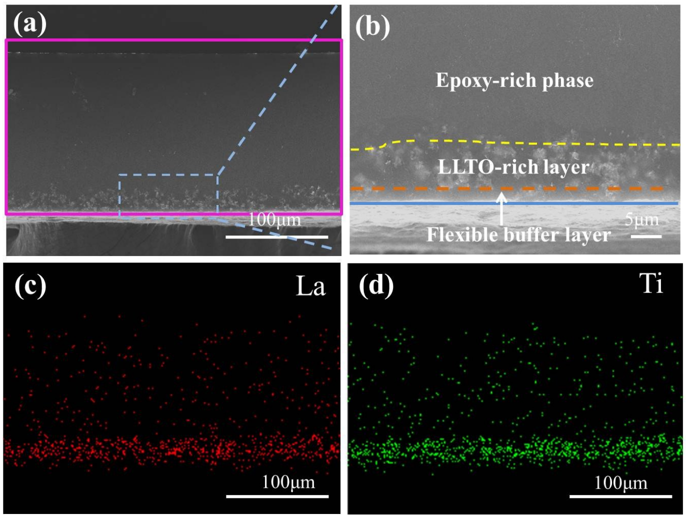

Fig. S10 SEM morphology for (a) the cross section of the c-EME-10% after cycling 100 cycles at 0.2C and (b) the interface between the three layers at a higher magnification. (c), (d) Corresponding EDS elemental mappings.

Table S3 The performance of various composite electrolytes

Type	Electrolyte	Ionic conductivity (S cm^{-1})	Li-ion transference number	current density /areal capacity in polarization test (mA cm^{-2})/ (mA h cm^{-2})	Short circuit time (h)	Capacity retention in $LiFePO_4$/Li LMBs	Coulombic efficiency	date
GPE/Separator	**DGEBA/LLTO nanoparticles**	**2.02×10^{-3} (25°C)**	**0.82**	**4 / 12**	**>600**	**98.6% after 100 cycles at 0.2 C (25°C)**	**99.9%**	**Our work**
				2 / 6	**>1000**			
	Biomimetic Ant-nest Ionogel Electrolyte	1.37×10^{-3} (30°C)	-	0.1 / 0.1	>600	Close to 100% after 10 cycles at 0.1 C (60°C)	99.8%	2017[3]
	PVDF-HFP crosslinked with epoxy resin	2.36×10^{-3} (25°C)	-	2.5 / 7.5	>250	99.3% after 200 cycles at 0.3 C (25°C)	99.5%	2017[4]
	3D Printable PVDF/Al_2O_3 nanoparticle	8.2×10^{-4}	-	0.1 / 1.5	>4000	97% after 100 cycles at 0.2 C	-	2017[5]

	s							
	PVdF/Hollow SiO$_2$/ Crosslinked TPGDA	1.74×10^{-3}(at room temperature)	0.44	1 / 3	>200	100.2% after 200 cycles at 0.2 C	-	2016[6]
	Crosslinked SiO2 nanoparticles with PS-PEO block copolymer	4.5×10^{-4} (at room temperature)	-	1 / 3	>120	91.7% after 140 cycles at 0.5 C	over 90%	2015[7]
	sandwich-type PVDF-HFP/nanoporous Al$_2$O$_3$/PVDF-HFP	1×10^{-3} (at room temperature)	-	0.2 / 0.4	>1000	73.7% after 100 cycles at 1 C	Close to 100%	2014[8]
Quasi-SPE/SPE	PVDF-HFP/LLZO particles	1.1×10^{-4} (25°C)	0.61	0.2 / 0.2	420	92.5% after 180 cycles at 0.5 C (25°C)	Close to 100%	2018[9]
	AlPO$_4$ nanoparticles /poly(tri-acrylate) network	3.75×10^{-3}	0.79	4 / 2	>200	85% after 200 cycles at 1 C (55°C)		2018[10]
	LATP/PAN /PEO	6.5×10^{-4} (60°C)	0.32	0.3 / 0.3	>400	95.6% after 100 cycles at 0.2 C (60°C)	99.5%	2018[11]
	Asymmetric Solid Electrolyte with Engineered Layers	1×10^{-4} (55°C)	-	0.1 / 1	>3200	94.5% after 120 cycles at 0.2 C (55°C)	99.8%	2017[12]
	Crosslinked PEG-POSS	9.5×10^{-5} (30°C)	-	1 / 3	441	95.8% after 50 cycles at 0.3 C (90°C)	＞99%	2015[13]

Notes and References

[1] E. D. H. Van, G. Maino, G. Bonneux, W. Marchal, K. Elen, S. Gielis, F. Mattelaer, C. Detavernier, P. H. L. Notten, M. K. V. Bael and A. Hardy, *Materials*, 2017, 10, 1072.

[2] K. Minami, A. Hayashi, S. Ujiie and M. Tatsumisago, *Solid State Ionics*, 2011, 192, 122-125.

[3] N. Chen, Y. J. Dai, Y. Xing, L. L. Wang, C. Guo, R. J. Chen, S. J. Guo and F. Wu, *Energy*

Environ. Sci., 2017, 10,1660-1667.

[4] Q. W. Lu, Y. B. He, Q. P. Yu, B. H. Li, Y. V. Kaneti, Y. W. Yao, F. Y. Kang and Q. H. Yang, *Adv. Mater*., 2017, 29, 1604460.

[5] A. J. Blake, R. R. Kohlmeyer, J. O. Hardin, E. A. Carmona, B. J. Maruyama, J. D. Berrigan H. Huang and M. F. Durstock, *Adv. Energy Mater*., 2017, 7, 1602920.

[6] D. Zhou, R. L. Liu, Y. B. He, F. Y. Li, M. Liu, B. H. Li, Q. H. Yang, Q. Cai and F. Y. Kang, *Adv. Energy Mater*., 2016, 6, 1502214.

[7] S. Choudhury, R. Mangal, A. Agrawal and L. A. Archer, *Nat. Commun*., 2015, 6, 10101.

[8] Z. Y. Tu, Y. Kambe, Y. Y. Lu and L. A. Archer, *Adv. Energy Mater*., 2014, 4, 1300654.

[9] W. Q. Zhang, J. H. Nie, F. Li, Z. L. Wang and C. W. Sun, *Nano. Energy*, 2018, 45, 413-419.

[10] X. X. Zeng, Y. X. Yin, Y. Shi, X. D. Zhang, H. R. Yao, R. Wen, X. W. Wu and Y. G. Guo, *Chem*, 2018, 4, 1-10.

[11] D. Li, L. Chen, T. S. Wang and L. Z. Fan, *ACS Appl. Mater. Interfaces*, 2018, 10, 7069-7078.

[12] H. Duan, Y. X. Yin, Y. Shi, P. F. Wang, X. D. Zhang, C. P. Yang, J. L. Shi, R. Wen, Y. G. Guo and L. *J. Wan, J. Am. Chem. Soc*., 2017, 140, 82-85.

[13] Q. W. Pan, D. M. Smith, H. Qi,. S. J. Wang and C. Y. Li, *Adv. Mater*., 2015, 27, 5995-6001.